

# Tunable superconducting flux qubits with long coherence times

T. Chang,<sup>1</sup> T. Cohen,<sup>1</sup> I. Holzman,<sup>1</sup> G. Catelani,<sup>2,3</sup> and M. Stern<sup>1</sup>

<sup>1</sup>*Quantum Nanoelectronics Laboratory, Department of Physics & Bar-Ilan Institute of Nanotechnology and Advanced Materials (BINA), 5290002 Ramat-Gan, Israel.*

<sup>2</sup>*JARA Institute for Quantum Information (PGI-11), Forschungszentrum Jülich, 52425 Jülich, Germany*

<sup>3</sup>*Quantum Research Centre, Technology Innovation Institute, Abu Dhabi, United Arab Emirates*

(Dated: 15 June 2022)

In this work, we study a series of tunable flux qubits inductively coupled to a coplanar waveguide resonator fabricated on a sapphire substrate. Each qubit includes an asymmetric superconducting quantum interference device which is controlled by the application of an external magnetic field and acts as a tunable Josephson junction. The tunability of the qubits is typically  $\pm 3.5$  GHz around their central gap frequency. The measured relaxation times are limited by dielectric losses in the substrate and can attain  $T_1 \sim 8 \mu\text{s}$ . The echo dephasing times are limited by flux noise even at optimal points and reach  $T_{2E} \sim 4 \mu\text{s}$ , almost an order of magnitude longer than state of the art.

The superconducting flux qubit is a micron-size superconducting aluminium loop intersected by several Josephson junctions, among which one is smaller than others by a factor  $\alpha$  [1–6]. When the flux threading the loop is close to half a flux quantum, this circuit behaves as a two-level system and can exhibit long coherence times [7, 8]. Thus, it is often considered as a strategic building block for the physical realization of superconducting quantum computers [9]. Yet, a good control of the transition energy of the qubit at its optimal working point is required to perform efficient gates on a scalable system.

A good strategy for controlling the qubit transition energy consists of replacing one of the junction by a superconducting quantum interference device (SQUID). The advantage of this approach is that another control parameter is added to the system: the flux  $\Phi_S$  threading the loop of the SQUID controls the critical current of the equivalent junction and therefore modifies the energy of the flux qubit while keeping it at its optimal point. This kind of design was implemented for the first time in Ref. [10]: a symmetric SQUID formed by two identical Josephson junctions was introduced at the position of the  $\alpha$ -junction in order to control the gap energy of the qubit. The results of this experiment were positive in terms of controllability ( $\sim 0.7$  GHz/m $\Phi_0$ ) but the relaxation and dephasing times of the qubit were severely degraded ( $T_1 \lesssim 1 \mu\text{s}$ ,  $T_2 \sim 10$  ns).

These short coherence times are generally attributed to the presence of flux noise in the SQUID loop [11, 12]. For any flux-tunable qubit, this flux noise leads to significant dephasing whenever the qubit energy is too strongly dependent on the external flux bias  $\Phi_S$ . A possible way to mitigate this issue consists of using an asymmetric SQUID formed by two different junctions having respectively a Josephson energy  $(1+d)E_J/2$  and  $(1-d)E_J/2$  with  $d \in [0, 1]$ . The equivalent Josephson energy of such a SQUID  $E_J(\Phi_S)$  varies according to the following expression [13]:

$$E_J(\Phi_S) = E_J \sqrt{\frac{(1+d^2) + (1-d^2) \cos\left(\frac{\Phi_S}{\varphi_0}\right)}{2}} \quad (1)$$

where  $\varphi_0 = \hbar/2e$ . For a given value of  $d$ , the function  $E_J(\Phi_S)$  ranges between  $dE_J$  and  $E_J$  and consequently the dependence of the qubit energy on  $\Phi_S$  is strongly reduced as  $d$  approaches 1. This technique has been demonstrated recently for tuning transmon qubits while keeping good coherence properties [14, 15].

In this work, we follow the same strategy for controlling the gap of superconducting flux qubits. We replace one of the unitary junctions of the flux qubit by an asymmetric SQUID and study the controllability of the qubits and their coherence properties. The tunability of the qubits is  $\pm 3.5$  GHz around their central frequency. The intrinsic relaxation rates can be as low as  $\Gamma_{int} \sim 130$  kHz ( $T_1 \sim 8 \mu\text{s}$ ) while the pure echo dephasing rates at optimal points are typically  $\Gamma_{\varphi E} \sim 260 \pm 90$  kHz ( $T_{2E}^{\varphi} \sim 4 \mu\text{s}$ ). These decoherence rates are much smaller than the state of the art for tunable flux qubits [10, 16, 17]. We show that these decoherence rates are mostly limited by flux noise, even at optimal points.

The sample studied in this work is presented in Fig. 1a. It is fabricated on a sapphire chip and contains a  $\lambda/2$  aluminium coplanar waveguide (CPW) resonator with two symmetric ports for microwave transmission measurements. The resonator has a first resonant mode at  $\omega_r/2\pi \sim 10.23$  GHz with quality factor  $Q \sim 3500$ . Five tunable flux qubits labelled according to their position on the resonator  $i = \{1, \dots, 5\}$  are galvanically coupled to the CPW resonator with coupling constant  $\sim 120$  MHz.

The qubits are fabricated by double angle-evaporation of Al–AlOx–Al using a tri-layer CSAR-Ge-MAA process [8]. The tri-layer is patterned by electron-beam lithography, developed and etched by a reactive ion etcher in order to form a suspended germanium mask. This mask is robust and evacuates efficiently the charges during e-beam lithography, and thus provides a good precision and reproducibility of the junction sizes. Before aluminium

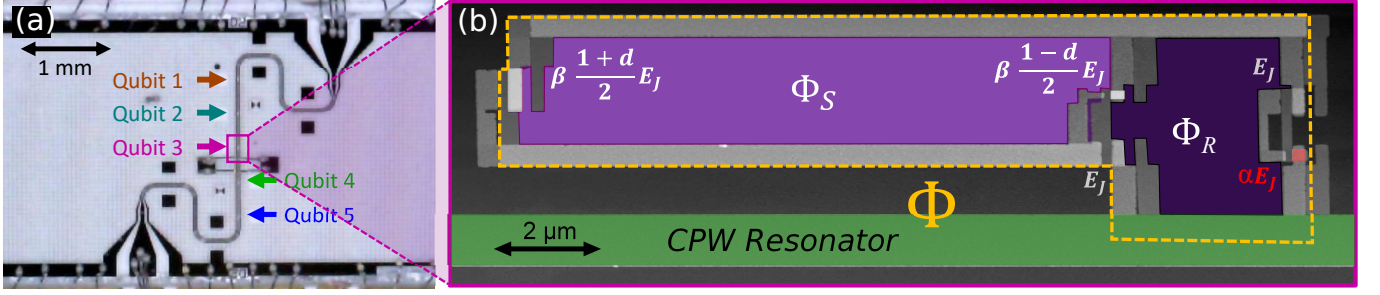


FIG. 1. (a) Microscope picture of the sample, showing the coplanar waveguide resonator inductively coupled to five tunable flux qubits labelled according to their position on the resonator. The resonator is fabricated on a sapphire wafer by evaporation of a 150 nm- thick aluminium layer and UV lithography. (b) Colored atomic force micrograph of flux qubit 3. The qubit is galvanically coupled to the central conductor of the resonator (colored in green). It consists of two loops: The surface of the main loop is  $S_{main}^{(3)} = 43.71 \mu\text{m}^2$  while the surface of the SQUID loop is  $S_{squad} = 30.82 \mu\text{m}^2$  giving a ratio  $\zeta^{(3)} = 0.705$ . In our experimental setup, the magnetic field is applied uniformly such that the flux threading the SQUID loop is  $\Phi_S = \zeta\Phi$  and  $\Phi_R = (1 - \zeta)\Phi$ .

evaporation, an ion milling step etches the oxide layer from the central conductor of the resonator in order to connect it galvanically to the qubit. A first 25 nm layer of aluminium is evaporated at  $-50^\circ\text{C}$  in a direction of  $-25^\circ$  relative to the sample axis. This step is followed by dynamic oxidation of  $\text{O}_2/\text{Ar}$  (15%-85%) at  $P = 20 \mu\text{bar}$  for a duration of 30 minutes. A second layer of 30 nm of aluminium is then evaporated with the opposite angle ( $25^\circ$ ) at a temperature of  $\sim 7^\circ\text{C}$ . The low temperature enables us to reduce the grain size of aluminium and to better control the dimensions and oxidation properties of our junctions. Before cooling down the sample, we performed room temperature measurements of reference junctions. An histogram of these measurements is given in Supplementary Materials [18].

The low temperature measurements of the qubits are performed in a cryogen-free dilution refrigerator at a temperature of 14 mK. The input line is attenuated at low temperature to minimize thermal noise and filtered with homemade impedance-matched radiation-absorbing filters. The readout output line includes a band-pass filter, a double circulator and a cryogenic amplifier. Qubit state manipulations are performed by injecting in the input line of the resonator microwave pulses at the frequency of the qubit  $\omega_{01}$ , followed by a readout pulse at  $\omega_r$  whose amplitude and phase yield the qubit excited state probability. The sample is glued on a printed circuit board and embedded into a superconducting coil that is used to provide magnetic flux biases to the qubits. In order to isolate the device from surrounding magnetic noise, the system is magnetically shielded with a Cryoperm box surrounding a superconducting enclosure.

Fig. 1b presents a colored atomic force micrograph (AFM) of one of these qubits. The circuit consists of two loops. The main loop indicated by a yellow dashed line is intersected by two identical Josephson junctions of Josephson energy  $E_J$  and one smaller junction colored in red of Josephson energy  $\alpha E_J$ . The SQUID loop is intersected by two additional Josephson junctions of

Josephson energy  $\beta(1+d)E_J/2$  and  $\beta(1-d)E_J/2$ . Its surface is smaller than the main loop by a factor  $\zeta \sim 0.7$ .

The inductive energy of the circuit exhibits two local minima which correspond to a persistent current  $I_P$  flowing clockwise or anticlockwise in the main loop. These two minima become degenerate when the flux threading the main loop  $\Phi = \Phi_{opt}$  is such that

$$\frac{\Phi_{opt}}{\varphi_0} - \frac{\Phi_S}{2\varphi_0} + \delta\varphi = k\pi \quad (2)$$

with  $k = \pm 1, \pm 3, \pm 5, \dots$  and  $\tan \delta\varphi = d \tan \left[ \frac{\Phi_S}{2\varphi_0} \right]$ . At these *optimal* points, the two quantum states hybridise into symmetric and antisymmetric superpositions and give rise to an energy splitting  $\hbar\Delta$  called the flux-qubit gap. In our experimental setup, the magnetic field is applied uniformly such that the flux threading the SQUID loop is  $\Phi_S = \zeta\Phi$ . One can therefore solve Eq. 2 and get the values of the fluxes  $\Phi_{opt}$  and  $\Phi_S$  at each optimal point. For different values of  $k$ , the value of the effective Josephson energy of the SQUID changes according to Eq. 1 and consequently, the value of the gap of each qubit depends on  $k$ . In the following, the gap of qubit  $i$  at each optimal point will be denoted as  $\Delta^{(i,k\pi)}$  and its associated persistent current as  $I_P^{(i,k\pi)}$ .

Fig. 2a shows the frequency dependence of qubit 3 on  $\Phi$  around the  $\pi$  and  $5\pi$  optimal points. The transition frequency of the qubit around each optimal point follows  $\omega_{01} = \sqrt{\Delta^2 + \varepsilon^2}$  with  $\varepsilon = 2I_P(\Phi - \Phi_{opt})/\hbar$ , yielding  $\Delta^{(3,\pi)}/2\pi = 4.48 \text{ GHz}$ ,  $I_P^{(3,\pi)} = 456 \text{ nA}$  and  $\Delta^{(3,5\pi)}/2\pi = 7.15 \text{ GHz}$ ,  $I_P^{(3,5\pi)} = 354 \text{ nA}$ . We repeat this procedure for the five qubits at their respective optimal points  $\pm\pi, \pm 3\pi, \pm 5\pi, \pm 7\pi, \pm 9\pi$  (See [18]).

Fig. 2b presents the gaps of qubits 3, 4 and 5 versus  $\Phi_S/\varphi_0$ . This data together with the persistent currents obtained for each optimal point [18] enables us to fit parameters of the model shown in Fig. 2c. In this model, the qubit consists of two superconducting loops intersected by five Josephson junctions. Each Josephson

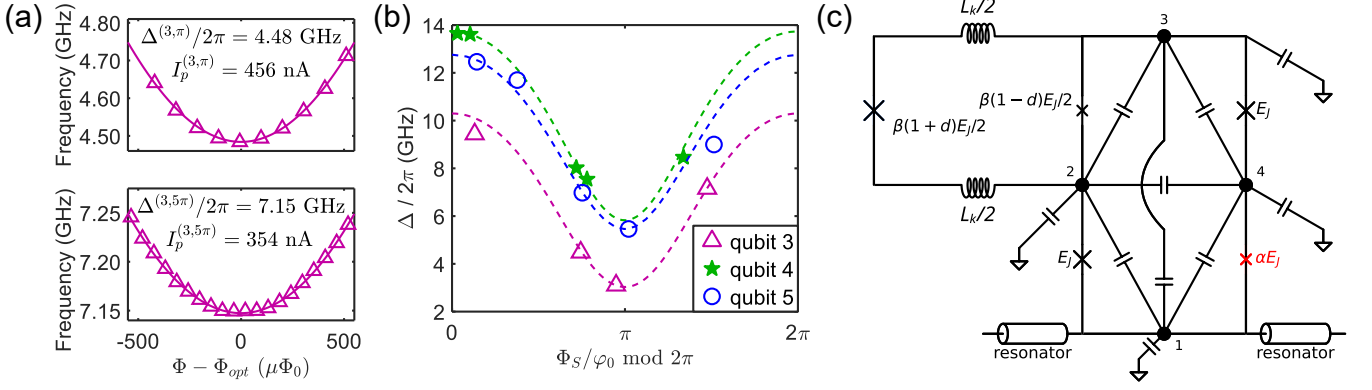


FIG. 2. (a) Measured qubit frequency of qubit 3 versus  $\Phi$  (magenta triangles) and fit (magenta curve) yielding the qubit parameters  $\Delta$  and  $I_p$  at optimal points  $\pi$  and  $5\pi$ . (b) Measured gaps of qubit 3 (magenta triangles), 4 (green stars) and 5 (blue circles) versus  $\Phi_S/\varphi_0$ . The dashed curves are calculated for arbitrary values of  $\Phi_S$  according to the model illustrated in (c) with fitting parameters  $E_J$ ,  $\alpha$  and  $d$ . (c) Flux qubit model including the kinetic inductance  $L_k$  and geometric capacitances. The island 1 is connected galvanically to the central conductor of the resonator.

Qubit #	$E_J$ (GHz)	$E_J/E_C$	$\alpha$	$d$	$\zeta$	$\sqrt{A_R A_S}$ ( $\mu\Phi_0$ )
1	550	318	0.429	0.759	0.696	2.2
2	558	323	0.426	0.715	0.687	2.6
3	559	323	0.442	0.711	0.705	2.3
4	518	300	0.421	0.707	0.677	2.3
5	563	326	0.426	0.740	0.714	3.0

TABLE I. Parameters of the qubits. The charging energy is fixed at  $E_C = 1.73$  GHz assuming a specific capacitance of the junction  $C/A = 100$  fF  $\mu\text{m}^{-2}$ . The ratio  $\zeta$  is measured by AFM. The value  $\beta = 2.11$  is taken according to room temperature measurements. The inductance  $L_k = 72.5$  pH is determined according to the resistance measurement of wires at low temperatures. The value of  $E_J$ ,  $d$  and  $\alpha$  are obtained by fit with the model shown in Fig. 2c. The amplitude of the flux noise  $\sqrt{A_R A_S}$  is extracted for each qubit from the dependence of  $\Gamma_{\varphi E}$  versus  $\varepsilon$ .

junction is characterized by its Josephson energy  $E_J$  and its bare capacitance energy  $E_C = e^2/2C_J$ . The junctions divide the loops into four superconducting islands. Each island is capacitively coupled to its surrounding by geometric capacitances. These geometric capacitances are calculated using the electrostatic module of COMSOL (see [18]). They reduce the gaps of the qubits by approximately  $\sim 1$  GHz but barely modify their persistent currents. It is also necessary to take into account the kinetic inductance of the SQUID loop in order to match the parameters of the model with the experimental results. The kinetic inductance is estimated by measuring the resistance of evaporated aluminium wires at low temperature and is added in our model as a renormalization of the large Josephson junction of the SQUID [18]. We summarize the results of the fits in Table 1. These values are in good agreement with the measured values of  $\alpha$ ,  $d$  and  $E_J$  extracted from room temperature resistance measurements (see [18]).

The change of the gap modifies the relaxation rate be-

tween the two qubit levels. For illustration, we represent in Fig. 3a the energy relaxation decay of qubit 3 at two different optimal points. The decay is exponential in both cases but the relaxation times are different, namely  $T_1^{(3,\pi)} = 7.7$   $\mu\text{s}$  and  $T_1^{(3,5\pi)} = 5.2$   $\mu\text{s}$ . Several mechanisms may give rise to such a phenomenon; among them, Purcell effect. The Purcell rate  $\Gamma_P$  is quantitatively determined by measuring the qubit Rabi frequency  $\Omega_R$  for a given microwave power  $P_{in}$  at the resonator input [8]. This enables us to analyze and compare the intrinsic relaxation rates defined as  $\Gamma_{int} = \Gamma_1 - \Gamma_P$  of all the qubits at various optimal points. Such an analysis shows that qubit 3 has approximately the same intrinsic relaxation rate at optimal points  $\pi$  and  $5\pi$ .

Fig. 3b unveils a general behavior of intrinsic relaxation rates versus frequency. Previous measurements of flux qubits [8] identified dielectric losses in the substrate as a major contributor to relaxation at low temperature [19]; using the approach of Ref. [8] and a loss tangent of  $5 \times 10^{-5}$ , we obtain the dashed line in Fig. 3b. Clearly dielectric losses account for most of the relaxation at intermediate frequencies but cannot explain the increased relaxation rates at high frequencies when the flux in the SQUID  $\Phi_S/\varphi_0$  is close to  $2\pi$ . A second source of losses could be quasiparticle tunneling [20–22]. A single quasiparticle trapped in one of the large qubit islands would lead to a relaxation rate larger than what is observed, at least at low frequencies, as well as to non-exponential decay due to fluctuations in the number of trapped quasiparticles [23, 24]. Alternatively, quasiparticles can reach the qubits from the CPW resonator. However, a relatively high normalized quasiparticle density, corresponding to an effective quasiparticle temperature of order 150 mK, would be needed to explain a decay rate of the order of tens of kHz. Therefore we conclude that quasiparticles do not significantly account for relaxation and cannot explain the residual decay rate observed

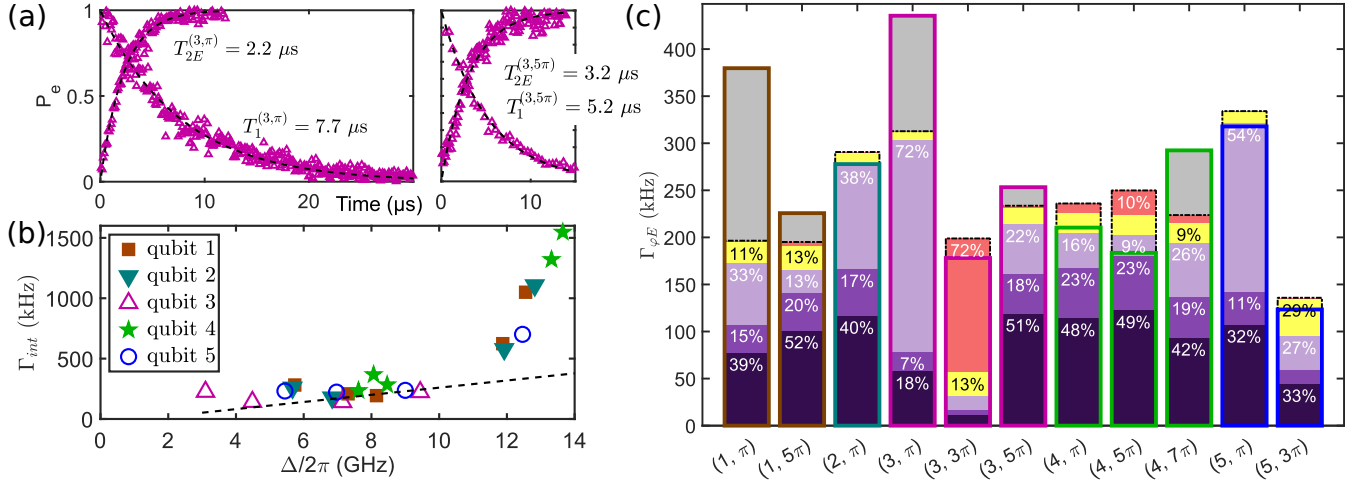


FIG. 3. (a) Energy relaxation and spin-echo measurements of qubit 3 at optimal points  $\pi$  and  $5\pi$ . (b) Intrinsic relaxation rates  $\Gamma_{int}$  versus  $\Delta$ . The dashed line corresponds to calculated dielectric losses in the substrate assuming  $\tan \delta = 5 \times 10^{-5}$ . (c) Stacked bar chart showing the measured pure echo dephasing rates  $\Gamma_{\phi E}^{(i,k\pi)}$ . The calculated contributions to dephasing are represented in different colors: flux noise (purple), critical current noise  $\Gamma_{\alpha}$  (yellow) and photon noise  $\Gamma_{phot}$  (red). The flux noise dephasing can be separated into first order flux noise in the qubit loop  $\Gamma_R$  (dark purple), first order flux noise in the SQUID loop  $\Gamma_S$  (purple) and second order effects  $\Gamma_{2nd}$  (light purple). The total  $\Gamma_{tot} = \sqrt{\Gamma_R^2 + \Gamma_S^2 + \Gamma_{2nd}^2 + \Gamma_{\alpha}^2 + \Gamma_{phot}^2}$  is represented as a dot-dashed black segment. For each contribution  $X \in \{R, S, 2nd, \alpha, phot\}$ , the percentage indicated in the relevant colored stack represents  $\Gamma_X^2/\Gamma_{tot}^2$ .

at high frequencies.

At their respective optimal points, the amplitude of the spin-echo signal shown in Fig. 3a decays with pure dephasing times  $T_{\phi E}^{(3,\pi)} = 2.6 \mu\text{s}$  and  $T_{\phi E}^{(3,5\pi)} = 4.6 \mu\text{s}$ . In Fig. 3c, we present a stacked bar chart showing the measured pure echo dephasing rates at various optimal points and the different contributions of flux noise, critical current noise, charge noise, and photon noise. The dephasing due to photon noise (represented in red) has been estimated by measuring the dispersive shifts at optimal points and by estimating the number of thermal photons in the resonator [4]. It is the dominant dephasing mechanism for  $(3, 3\pi)$  since at that point the qubit gap happens to be very close to the resonator transition. The contribution of charge noise is strongly reduced by the ratio  $E_J/E_C \sim 300$  and was found to be always completely negligible ( $< 1$  kHz). We also considered critical current fluctuations in the  $\alpha$  junction assuming  $S_{I_{\alpha}}(\omega) = A_{I_{\alpha}}^2/|\omega|$ , with  $A_{I_0} \sim 0.1$  pA [25, 26], and found an approximately constant contribution of  $\sim 70$  kHz (represented in yellow in Fig. 3c). The flux noise shown in purple represents the main source of dephasing of the qubits even at optimal points.

Away from their optimal points, the decoherence of flux qubits is known to be governed by flux noise [5, 7, 8]. The flux noise power spectrum  $S_{\Phi}(\omega) = A_{\Phi}^2/|\omega|$  implies that the pure echo dephasing rate is given by  $\Gamma_{\phi E}^{\Phi} = A_{\Phi} \sqrt{\ln 2} |\partial\omega_0/\partial\Phi|$  with  $|\partial\omega_0/\partial\Phi| \simeq 2 I_P |\varepsilon|/\hbar\Delta$  [27]. At the optimal points,  $\varepsilon = 0$  and thus this decoherence mechanism should be cancelled. Yet, contrary to *standard* flux qubits, our design contains two independent de-

grees of freedom ( $\Phi_S, \Phi_R$ ) [16]. These degrees of freedom add  $\sigma_z$  components in the Hamiltonian of the system, namely  $\mathcal{H} = \hbar\frac{\Delta}{2}\sigma_z + (I_{z,S}\delta\Phi_S + I_{z,R}\delta\Phi_R)\sigma_z$  (See [18]). Thus, even at optimal point where  $I_{z,S}\zeta + I_{z,R}(1-\zeta) = 0$ ,  $\partial\omega_0/\partial\Phi_{S/R} \neq 0$  will give first order contributions to dephasing:

$$\Gamma_{S/R} = 2\sqrt{\ln 2} \frac{I_{z,S/R} A_{S/R}}{\hbar} \quad (3)$$

For each qubit, we measure  $\Gamma_{\phi E}$  versus  $\varepsilon$  and extract the apparent flux noise amplitude  $A_{\Phi}$  around each optimal point. The amplitudes  $A_{S/R}$  of the flux noise in the different loops can be directly extracted from  $A_{\Phi}$  and from the ratio  $\gamma = \sqrt{P_S/P_R}$  where  $P_S$  and  $P_R$  are the perimeters of the two loops [12]. As expected, we find that  $A_S$  and  $A_R$  do not change significantly for the different optimal points of a given qubit and thus  $\sqrt{A_S A_R}$  is a good indicator of flux noise in each qubit (See Table 1). A more rigorous derivation of flux noise contributions including second order effects is given in [18]. We find that such effects can be also significant as shown in Fig. 3c.

In conclusion, we have shown that it is possible to control the gap of flux qubits by using an asymmetric SQUID. This method mitigates the decoherence due to flux noise in the SQUID loop while keeping a tunability range of  $\pm 3.5$  GHz. It should be possible to improve further the coherence properties of the qubits by reducing the persistent currents down to 200 nA and by exchanging the locations of the small and large junctions of the SQUID. This exchange will further reduce the tunability

of the qubit to the level of  $\pm 500$  MHz and thus decrease the pure dephasing rates related to the presence of the SQUID. According to our simulations, the dephasing rate due to flux noise should then be comprised between 15 and 100 kHz.

963/19. G.C. acknowledges support by the German Federal Ministry of Education and Research (BMBF), funding program *Quantum technologies - from basic research to market*, project QSolid (Grant No. 13N16149).

## ACKNOWLEDGMENTS

This research was supported by the Israeli Science Foundation under grant numbers 426/15, 898/19 and

T. Chang and T. Cohen contributed equally to this work.

# Supplementary Materials

## I. TUNABLE FLUX QUBIT MODEL

In the model shown in Fig. 2c, the circuit consists of two superconducting loops intersected by five Josephson junctions. Each Josephson junction is characterized by its Josephson energy  $E_J$  and its bare capacitance energy  $E_C = e^2/2C_J$ . The junctions divide the loops into four superconducting islands. The island 1 is galvanically connected to the coplanar waveguide resonator. Each island is capacitively coupled to its surrounding by geometric capacitances. We take also into account the kinetic inductance of the SQUID loop. This kinetic inductance can be considered in a first approximation as a renormalization of the large Josephson junction of the SQUID as will be shown hereinbelow.

### A. Treating the kinetic inductance as a renormalization

The kinetic inductance of the SQUID loop is represented in the circuit of Fig. 2c as a an inductor of inductance  $L_k$  in series with the large SQUID junction. To find the renormalized parameters for this junction, we treat it as a linear element with admittance

$$Y_J(\omega) = \frac{1}{i\omega L_J} + i\omega C_J = \frac{1 - (\omega/\omega_p)^2}{i\omega L_J} \quad (4)$$

with  $\omega_p = 1/\sqrt{L_J C_J}$  the plasma frequency of the junction. Adding the kinetic inductance in series, we find for the total admittance:

$$Y_t(\omega) = \left( i\omega L_k + \frac{i\omega L_J}{1 - (\omega/\omega_p)^2} \right)^{-1} = \frac{1 - (\omega/\omega_p)^2}{i\omega L_J + i\omega L_k(1 - (\omega/\omega_p)^2)} \quad (5)$$

For frequencies small compared to the plasma frequency, the expansion of this formula at first order in  $(\omega/\omega_p)^2$  gives

$$Y_t(\omega) \simeq \frac{1 - (\omega/\omega_p)^2 \frac{L_J}{L_J + L_k}}{i\omega(L_J + L_k)} \quad (6)$$

Comparing the right-hand sides of Eqs.(4) and (6), we see that the latter can be obtained from former upon the replacements

$$\begin{aligned} L_J &\rightarrow L_J + L_k = L_J(1 + \eta) \\ C_J &\rightarrow C_J \left( \frac{L_J}{L_J + L_k} \right)^2 = \frac{C_J}{(1 + \eta)^2} \end{aligned}$$

where we introduced the dimensionless parameter  $\eta = L_k/L_J$ . In our model we use these replacement to take into account the kinetic inductance of the SQUID loop.

### B. Potential Energy

The potential energy of the circuit corresponds to the inductive energy of the junctions and can be written as

$$U = -E_J \cos \varphi_{12} - \beta \frac{1+d}{2(1+\eta)} E_J \cos \varphi_{23} - \beta \frac{1-d}{2} E_J \cos \varphi'_{23} - E_J \cos \varphi_{23} - \alpha E_J \cos \varphi_{41}$$

where  $\varphi_{j,k}$  denotes the phase difference  $\varphi_k - \varphi_j$  between islands  $j$  and  $k$ .

Introducing

$$\begin{aligned}\bar{\beta} &= \beta \left( \frac{1+d}{2(1+\eta)} + \frac{1-d}{2} \right) \\ \bar{d} &= \frac{(2+\eta)d - \eta}{-\eta d + (2+\eta)}\end{aligned}$$

enables us to write the potential energy under the form

$$U = -E_J \cos \varphi_{12} - \bar{\beta} \frac{1+\bar{d}}{2} E_J \cos \varphi_{23} - \bar{\beta} \frac{1-\bar{d}}{2} E_J \cos \varphi'_{23} - E_J \cos \varphi_{23} - \alpha E_J \cos \varphi_{41} \quad (7)$$

Faraday law implies that

$$\varphi_{41} = \frac{\Phi}{\varphi_0} - \sum_{j=1}^3 \varphi_{j,j+1} \quad (8)$$

$$\varphi'_{23} = \varphi_{23} - \frac{\Phi_S}{\varphi_0} \quad (9)$$

where  $\Phi$  is the flux threading the qubit loop,  $\Phi_S$  is the flux threading the SQUID loop and  $\varphi_0 = \hbar/2e$ .

One can write

$$\begin{aligned}& \bar{\beta} \frac{1+\bar{d}}{2} E_J \cos \varphi_{23} + \bar{\beta} \frac{1-\bar{d}}{2} E_J \cos \varphi'_{23} \\ &= \bar{\beta} E_J \sqrt{\frac{(1+\bar{d}^2) + (1-\bar{d}^2) \cos\left(\frac{\Phi_S}{\varphi_0}\right)}{2}} \cos\left(\varphi_{23} - \frac{\Phi_S}{2\varphi_0} + \arctan\left(\bar{d} \tan\left[\frac{\Phi_S}{2\varphi_0}\right]\right)\right)\end{aligned} \quad (10)$$

At optimal point, the sum of the phases across all junctions (including the SQUID effective junction) should be a odd multiple of  $\pi$ . We thus obtain the condition for optimal points given by Eq.2 of the main text

$$\boxed{\frac{\Phi_{opt}}{\varphi_0} - \frac{\Phi_S}{2\varphi_0} + \overline{\delta\varphi} = k\pi}$$

with  $k = \pm 1, \pm 3, \pm 5, \dots$  and  $\tan \overline{\delta\varphi} = \bar{d} \tan\left[\frac{\Phi_S}{2\varphi_0}\right]$ .

### C. Kinetic Energy

The kinetic energy  $K$  of the system is the sum of the capacitive energies of the circuit

$$K = \frac{1}{2} \sum_{i \neq j} C_{ij} (V_j - V_i)^2 + \frac{1}{2} C_J \left( (V_1 - V_2)^2 + \beta' (V_2 - V_3)^2 + (V_3 - V_4)^2 + \alpha (V_4 - V_1)^2 \right) \quad (11)$$

where  $C_{ij}$  is the capacitance between islands  $i$  and  $j$  and  $\beta' = \beta \left( \frac{1+d}{2(1+\eta)^2} + \frac{1-d}{2} \right)$  according to I A. It is a quadratic form of the island voltages  $V_i$  and can thus be written as

$$K = \frac{1}{2} \mathbf{V}^T \mathbf{C} \mathbf{V} \quad (12)$$

where  $\mathbf{V}^T = (V_1, V_2, V_3, V_4)$  and  $\mathbf{C}$  is a  $4 \times 4$  matrix which we will refer in the following as the capacitance matrix. The matrix  $\mathbf{C}$  can be written as the sum of the Josephson capacitance matrix  $\mathbf{C}_J$  and the geometric capacitance matrix  $\mathbf{C}_{\text{geom}}$ :

$$\mathbf{C} = \mathbf{C}_J + \mathbf{C}_{\text{geom}} \quad (13)$$

where

$$\mathbf{C}_J = C_J \begin{pmatrix} 1+\alpha & -1 & 0 & -\alpha \\ -1 & 1+\beta' & -\beta' & 0 \\ 0 & -\beta' & 1+\beta' & -1 \\ -\alpha & 0 & -1 & 1+\alpha \end{pmatrix} \quad (14)$$

and

$$\mathbf{C}_{\text{geom}} = \begin{pmatrix} C_{10} + \sum_{j \neq 1} C_{1j} & -C_{12} & -C_{13} & -C_{14} \\ -C_{21} & C_{20} + \sum_{j \neq 2} C_{2j} & -C_{23} & -C_{24} \\ -C_{31} & -C_{32} & C_{30} + \sum_{j \neq 3} C_{3j} & -C_{34} \\ -C_{41} & -C_{42} & -C_{43} & C_{40} + \sum_{j \neq 4} C_{4j} \end{pmatrix} \quad (15)$$

We determined the geometric capacitance matrix  $\mathbf{C}_{\text{geom}}$  using an electrostatic simulator (COMSOL) and find

$$\mathbf{C}_{\text{geom}} = \begin{pmatrix} 25.0000 & -0.8329 & -0.4047 & -0.1476 \\ -0.8329 & 1.8569 & -0.6369 & -0.0063 \\ -0.4047 & -0.6369 & 1.9831 & -0.1700 \\ -0.1476 & -0.0063 & -0.1700 & 0.3541 \end{pmatrix} \quad \text{fF}$$

#### D. Pseudo-Hamiltonian

We write the Hamiltonian using Legendre transformation and diagonalize it. We obtain the spectrum of the flux qubit by subtracting the energy of the first excited state  $|1\rangle$  from the energy of the ground state  $|0\rangle$ . Close to the optimal points, the system behaves as a two level system. In the vicinity of each optimal point, the Hamiltonian of the system can be written perturbatively as

$$\begin{aligned} \mathcal{H} &= \mathcal{H}_0 - \partial_\Phi \left( \alpha E_J \cos \left( \frac{\Phi}{\varphi_0} - \sum_{j=1}^3 \varphi_{j,j+1} \right) + \bar{\beta} \frac{1-\bar{d}}{2} \cos \left( \varphi_{23} - \frac{\zeta \Phi}{\varphi_0} \right) \right)_{\Phi=\Phi_{opti}} \cdot (\Phi - \Phi_{opt}) \\ &= \mathcal{H}_0 + I_0 \left[ \alpha \sin(\varphi_{41}) - \zeta \bar{\beta} \frac{1-\bar{d}}{2} \sin(\varphi'_{23}) \right] (\Phi - \Phi_{opt}) \equiv \mathcal{H}_0 + \hat{I} \cdot (\Phi - \Phi_{opt}) \end{aligned} \quad (16)$$

When the current operator is projected on the eigenstates  $|0\rangle, |1\rangle$  of  $\mathcal{H}_0$  we get

$$\begin{aligned} \langle 0 | \hat{I} | 0 \rangle &= \langle 1 | \hat{I} | 1 \rangle \\ \langle 0 | \hat{I} | 1 \rangle &= \langle 1 | \hat{I} | 0 \rangle \equiv I_p \end{aligned} \quad (17)$$

Therefore, the Hamiltonian of the system can be written in this basis under the form

$$\mathcal{H}_{\text{eff}} = \frac{\hbar}{2} [\Delta \sigma_z + \varepsilon \sigma_x] \quad (18)$$

where  $\varepsilon = \frac{2I_p}{\hbar} (\Phi - \Phi_{opti})$ .

## II. FLUX NOISE IN THE TUNABLE FLUX QUBIT

In the following we consider flux noise originating from the SQUID loop and the remaining loop as two independent noise sources. In order to estimate their influence on the coherence of the qubits, we will treat the Hamiltonian perturbatively versus the variables  $\Phi_S$  and  $\Phi_R = \Phi - \Phi_S$  around an optimal point.

$$\begin{aligned}
\mathcal{H} &= \mathcal{H}_0 - E_J \partial_{\Phi_S} \left( \alpha \cos \left( \frac{\Phi_R + \Phi_S}{\varphi_0} - \sum_{j=1}^3 \varphi_{j,j+1} \right) + \bar{\beta} \frac{1 - \bar{d}}{2} \cos \left( \varphi_{23} - \frac{\Phi_S}{\varphi_0} \right) \right)_{\Phi=\Phi_{opti}} \delta\Phi_S \\
&\quad - E_J \partial_{\Phi_R} \left( \alpha \cos \left( \frac{\Phi_R + \Phi_S}{\varphi_0} - \sum_{j=1}^3 \varphi_{j,j+1} \right) \right)_{\Phi=\Phi_{opti}} \delta\Phi_R \\
&= \mathcal{H}_0 + I_0 \left( \alpha \sin(\varphi_{41}) - \bar{\beta} \frac{1 - \bar{d}}{2} \sin(\varphi'_{23}) \right) \delta\Phi_S + I_0 \alpha \sin(\varphi_{41}) \delta\Phi_R \\
&\equiv \mathcal{H}_0 + \hat{I}_S \delta\Phi_S + \hat{I}_R \delta\Phi_R
\end{aligned} \tag{19}$$

One can express the operators  $\hat{I}_{S/R}$  in the basis of the two lowest eigenstates of  $\mathcal{H}_0$  as  $\hat{I}_{S/R} = I_{x,S/R} \sigma_x + I_{z,S/R} \sigma_z + I_{0,S/R} \mathbb{1}$  and thus write the Hamiltonian as

$$\mathcal{H} = \hbar \frac{\Delta}{2} \sigma_z + (I_{z,S} \delta\Phi_S + I_{z,R} \delta\Phi_R) \sigma_z + (I_{x,S} \delta\Phi_S + I_{x,R} \delta\Phi_R) \sigma_x \tag{20}$$

The transition frequency of the qubit can be written as

$$\hbar\omega_{01} \simeq \hbar\Delta + 2I_{z,S} \delta\Phi_S + 2I_{z,R} \delta\Phi_R + \frac{1}{2\hbar\Delta} (2I_{x,S} \delta\Phi_S + 2I_{x,R} \delta\Phi_R)^2 \tag{21}$$

Since the flux noise has a 1/f spectrum, one can show that the first and second order contributions to dephasing are given by [27]

$$\begin{aligned}
\Gamma_{S/R} &= \sqrt{\ln 2} A_{S/R} |\partial_{\Phi_{S/R}} \omega_{01}| \\
\Gamma_{2nd,S/R} &\approx 2.3 A_{S/R}^2 \partial_{\Phi_{S/R}}^2 \omega_{01}
\end{aligned} \tag{22}$$

where  $A_S$  and  $A_R$  are the flux noise amplitudes in the SQUID and in the remaining loop respectively.

$$\begin{aligned}
\partial_{\Phi_{S/R}} \omega_{01} &= \frac{2I_{z,S/R}}{\hbar} + \frac{1}{\hbar^2 \Delta} (2I_{x,S} \delta\Phi_S + 2I_{x,R} \delta\Phi_R) (2I_{x,S/R}) \\
\partial_{\Phi_{S/R}}^2 \omega_{01} &= \frac{1}{\hbar^2 \Delta} (2I_{x,S/R})^2
\end{aligned}$$

An interesting property of 1/f noise is that the decay is Gaussian for first order contributions. And thus one can write

$$\Gamma_{1st} = \sqrt{(\Gamma_S)^2 + (\Gamma_R)^2} = \sqrt{\ln 2 \left( A_S^2 (\partial_{\Phi_S} \omega_{01})^2 + A_R^2 (\partial_{\Phi_R} \omega_{01})^2 \right)} \equiv A_\Phi \sqrt{\ln 2} |\partial_{\Phi} \omega_{01}| \tag{23}$$

where  $A_\Phi$  is the *apparent* measure of flux noise when the tunable qubit is biased by an external uniform magnetic field (see Fig. 1a). Due to the geometrical configuration,  $\Phi_S = \zeta \Phi$  and  $\Phi_R = (1 - \zeta) \Phi$  and thus

$$\partial_{\Phi_{S/R}} \omega_{01} = \underbrace{\frac{2I_{z,S/R}}{\hbar}}_{I_{z,S/R} \ll I_{x,S/R}} + \frac{1}{\hbar^2 \Delta} (2I_{x,S} \zeta + 2I_{x,R} (1 - \zeta)) (2I_{x,S/R}) \delta\Phi$$

Since  $\hat{I} = \zeta \hat{I}_S + (1 - \zeta) \hat{I}_R$  (see 19), we have  $I_P = \zeta I_{x,S} + (1 - \zeta) I_{x,R}$  and thus using 23, we get

$$A_\Phi I_P = \sqrt{A_S^2 I_{x,S}^2 + A_R^2 I_{x,R}^2} \tag{24}$$



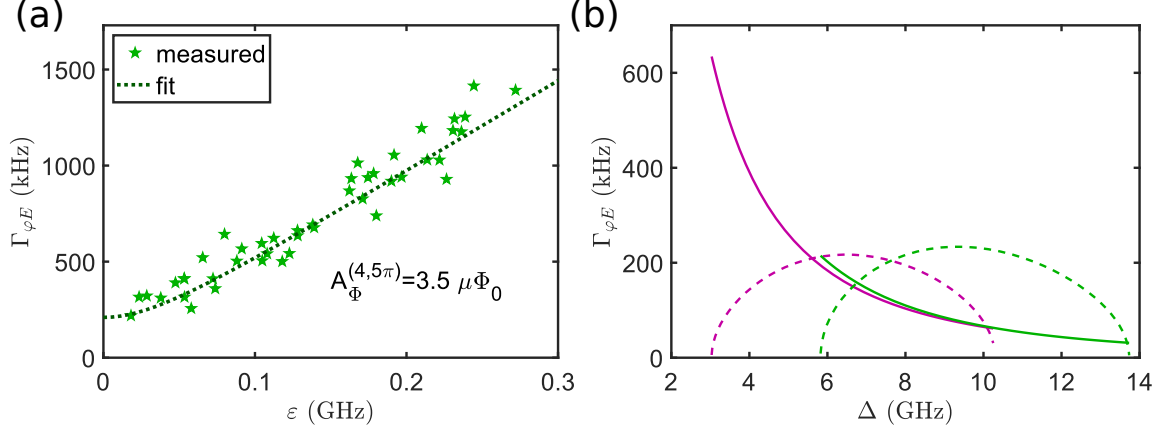


FIG. 4. (a) Measured pure dephasing rate  $\Gamma_{\varphi E}^{(4,5\pi)}$  versus  $\varepsilon$ . We extract the apparent flux noise amplitude from the slope of the graph using 23. (b) Calculated contribution of first (dashed line) and second order (solid line) flux noise to the dephasing rates for qubits 3 (magenta) and 4 (green) at optimal point. The curves are calculated for arbitrary values of  $\Phi_S$  while keeping the qubit at its optimal point.

Following Ref [12], we assume that the flux noise amplitude is proportional to the square root of the perimeters  $\sqrt{P_{S/R}}$  of the respective sections and define  $\gamma \equiv \sqrt{P_S/P_R} = A_S/A_R$  such that

$$A_S A_R = \frac{A_\Phi^2 I_P^2}{I_{x,S}^2 \gamma + I_{x,R}^2 / \gamma}$$

Finally we get

$$\Gamma_{1st} = 2\sqrt{\ln 2} \frac{\sqrt{A_S A_R}}{\hbar} \sqrt{\left(I_{z,S} + I_{x,S} \frac{2I_P}{\hbar \Delta} \delta\Phi\right)^2 \gamma + \left(I_{z,R} + I_{x,R} \frac{2I_P}{\hbar \Delta} \delta\Phi\right)^2 / \gamma}$$

$$\Gamma_{2nd} \approx 9.2 \frac{A_S A_R}{\hbar^2 \Delta} (I_{x,S}^2 \gamma + I_{x,R}^2 / \gamma)$$

In 4b, we represent the calculated contributions of first and second order flux noise to the dephasing rates for qubits 3 and 4 at optimal point when the flux  $\Phi_S/\varphi_0$  is varied between 0 and  $2\pi$ . The first order contributions are cancelled when the  $\partial_{\Phi_S} \omega_{01} = 0$  and reach a maximum of around 200 kHz approximately. The second order contributions are small for large gap and tend to become dominant when the flux qubit gap is small.

### III. ROOM TEMPERATURE MEASUREMENTS OF TEST JUNCTIONS

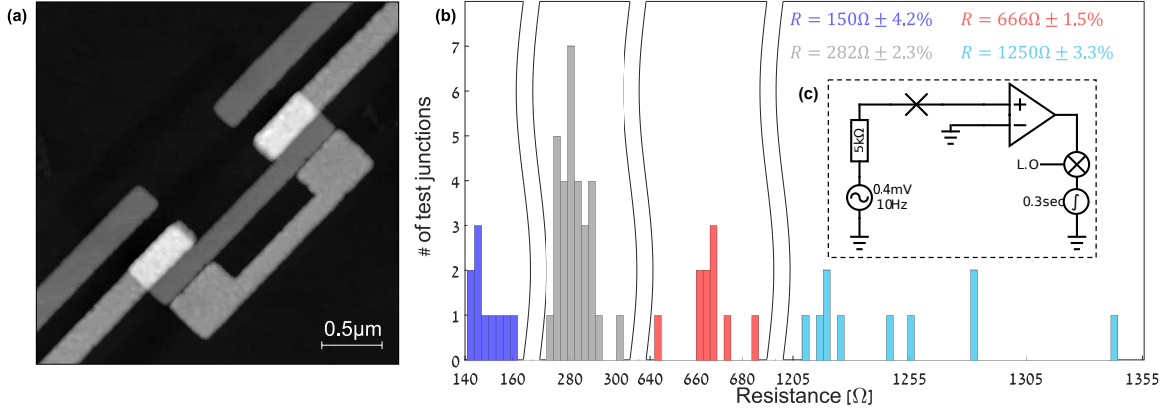


FIG. 5. (a) Atomic force micrograph of two unitary test junctions in series. (b) Histogram representing the resistance distribution of an ensemble of 60 test junctions: 30 unitary junctions (gray), ten  $\alpha$  junctions (red), ten  $\beta(1+d)/2$  junctions (dark blue), and ten  $\beta(1-d)/2$  junctions (light blue). (c) Scheme of the room temperature lock-in measurement setup.

The IV measurements have been performed using two-probe measurement. The probe station is connected in series with a 5 kΩ resistor to an A.C. output voltage of amplitude 4 mV at a frequency of 10.19 Hz. The current passing through the junction is measured by a lock-in amplifier with an integration time of 300 ms.

In 5b, we present a histogram showing the resistance distribution of the test junctions. The statistics of the test junctions presented in 5b were taken from 60 test junctions evaporated simultaneously with the sample. The standard deviations of the resistances are in the range of 1.5% ~ 4.2%. Using these measurements, we extract the parameters of the qubit  $\alpha = 0.42 \pm 0.01$ ,  $d = 0.79 \pm 0.01$  and  $\beta = 2.11 \pm 0.09$ . The critical current of the unitary junction can be estimated by Ambegaokar-Baratoff relation to be 1.08 μA.

### IV. QUBIT PARAMETERS

		$\pi$	$3\pi$	$5\pi$	$7\pi$	$9\pi$	Units
qubit 1	$\Delta/2\pi$	7.30	12.16	8.15	6.05	11.96	GHz
	$I_P$	376	230	342	401	230	nA
	$\chi/2\pi$	5.05	-5.93	6.37	3.16	-6.26	MHz
qubit 2	$\Delta/2\pi$	6.84	12.82	9.82	5.60	11.91	GHz
	$I_P$	388	238	282	440	263	nA
	$\chi/2\pi$	3.61	-4.31	33.1	3.41	-4.31	MHz
qubit 3	$\Delta/2\pi$	4.48	9.43	7.15	3.10	NaN	GHz
	$I_P$	457	289	354	NaN	NaN	nA
	$\chi/2\pi$	2.85	16.3	5.65	3.06	NaN	MHz
qubit 4	$\Delta/2\pi$	8.02	13.65	8.46	7.54	13.61	GHz
	$I_P$	365	224	353	341	246	nA
	$\chi/2\pi$	8.86	-4.66	11.3	8.21	-4.05	MHz
qubit 5	$\Delta/2\pi$	6.98	12.46	9.00	5.46	11.69	GHz
	$I_P$	392	254	332	444	NaN	nA
	$\chi/2\pi$	2.83	-4.08	6.48	NaN	-4.23	MHz

TABLE II. Qubit Parameters:  $\Delta$ ,  $I_P$  and the dispersive shift of the resonator  $\chi$ .

		$\pi$	$3\pi$	$5\pi$	$7\pi$	$9\pi$	Units
qubit 1	$\Gamma_1$	236	1073	271	296	647	kHz
	$\Gamma_P$	28	23	77	14	23	kHz
	$\Gamma_{int}$	208	1050	194	282	624	kHz
qubit 2	$\Gamma_1$	194	1141	NaN	268	625	kHz
	$\Gamma_P$	16	34	NaN	9	47	kHz
	$\Gamma_{int}$	178	1107	NaN	259	578	kHz
qubit 3	$\Gamma_1$	142	373	185	225	NaN	kHz
	$\Gamma_P$	1	151	45	0	NaN	kHz
	$\Gamma_{int}$	141	222	140	225	NaN	kHz
qubit 4	$\Gamma_1$	446	1858	341	298	1568	kHz
	$\Gamma_P$	79	310	58	62	248	kHz
	$\Gamma_{int}$	367	1548	283	236	1320	kHz
qubit 5	$\Gamma_1$	236	709	298	236	NaN	kHz
	$\Gamma_P$	14	8	60	5	NaN	kHz
	$\Gamma_{int}$	222	701	238	231	NaN	kHz

TABLE III. Relaxation Rates: measured relaxation rate  $\Gamma_1$ , estimated Purcell rate  $\Gamma_P$ , and the estimated intrinsic rate  $\Gamma_{int} = \Gamma_1 - \Gamma_P$ .

- 
- [1] T. P. Orlando, J. E. Mooij, Lin Tian, Caspar H. van der Wal, L. S. Levitov, Seth Lloyd, and J. J. Mazo. Superconducting persistent-current qubit. *Phys. Rev. B*, 60:15398–15413, Dec 1999.
- [2] J. E. Mooij, T. P. Orlando, L. Levitov, Lin Tian, Caspar H. van der Wal, and Seth Lloyd. Josephson persistent-current qubit. *Science*, 285(5430):1036–1039, August 1999.
- [3] I. Chiorescu, Y. Nakamura, C. J. P. M. Harmans, and J. E. Mooij. Coherent quantum dynamics of a superconducting flux qubit. *Science*, 299(5614):1869–1871, March 2003.
- [4] P. Bertet, I. Chiorescu, G. Burkard, K. Semba, C. J. P. M. Harmans, D. P. DiVincenzo, and J. E. Mooij. Dephasing of a superconducting qubit induced by photon noise. *Phys. Rev. Lett.*, 95:257002, Dec 2005.
- [5] F. Yoshihara, K. Harrabi, A. O. Niskanen, Y. Nakamura, and J. S. Tsai. Decoherence of flux qubits due to  $1/f$  flux noise. *Phys. Rev. Lett.*, 97:167001, Oct 2006.
- [6] J.-L. Orgiazzi, C. Deng, D. Layden, R. Marchildon, F. Ktapli, F. Shen, M. Bal, F. R. Ong, and A. Lupascu. Flux qubits in a planar circuit quantum electrodynamics architecture: Quantum control and decoherence. *Phys. Rev. B*, 93:104518, Mar 2016.
- [7] Jonas Bylander, Simon Gustavsson, Fei Yan, Fumiki Yoshihara, Khalil Harrabi, George Fitch, David G. Cory, Yasunobu Nakamura, Jaw-Shen Tsai, and William D. Oliver. Noise spectroscopy through dynamical decoupling with a superconducting flux qubit. *Nature Physics*, 7(7):565–570, May 2011.
- [8] M. Stern, G. Catelani, Y. Kubo, C. Grezes, A. Bienfait, D. Vion, D. Esteve, and P. Bertet. Flux qubits with long coherence times for hybrid quantum circuits. *Phys. Rev. Lett.*, 113:123601, Sep 2014.
- [9] I. Ozfidan, C. Deng, A.Y. Smirnov, T. Lanting, R. Harris, L. Swenson, J. Whittaker, F. Altomare, M. Babcock, C. Baron, A.J. Berkley, K. Boothby, H. Christiansi, P. Bunyk, C. Enderud, B. Evert, M. Hager, A. Haja, J. Hilton, S. Huang, E. Hoskinson, M.W. Johnson, K. Jooya, E. Ladizinsky, N. Ladizinsky, R. Li, A. MacDonald, D. Marsden, G. Marsden, T. Medina, R. Molavi, R. Neufeld, M. Nissen, M. Norouzpour, T. Oh, I. Pavlov, I. Perminov, G. Poulin-Lamarre, M. Reis, T. Prescott, C. Rich, Y. Sato, G. Sterling, N. Tsai, M. Volkmann, W. Wilkinson, J. Yao, and M.H. Amin. Demonstration of a nonstoquastic hamiltonian in coupled superconducting flux qubits. *Phys. Rev. Applied*, 13:034037, Mar 2020.
- [10] F. G. Paauw, A. Fedorov, C. J. P. M Harmans, and J. E. Mooij. Tuning the gap of a superconducting flux qubit. *Phys. Rev. Lett.*, 102:090501, Mar 2009.
- [11] C. M. Quintana, Yu Chen, D. Sank, A. G. Petukhov, T. C. White, Dvir Kafri, B. Chiaro, A. Megrant, R. Barends, B. Campbell, Z. Chen, A. Dunsworth, A. G. Fowler, R. Graff, E. Jeffrey, J. Kelly, E. Lucero, J. Y. Mutus, M. Neeley, C. Neill, P. J. J. O’Malley, P. Roushan, A. Shabani, V. N. Smelyanskiy, A. Vainsencher, J. Wenner, H. Neven, and John M. Martinis. Observation of classical-quantum crossover of  $1/f$  flux noise and its

- paramagnetic temperature dependence. *Phys. Rev. Lett.*, 118:057702, Jan 2017.
- [12] Jochen Braumüller, Leon Ding, Antti P. Vepsäläinen, Youngkyu Sung, Morten Kjaergaard, Tim Menke, Roni Winik, David Kim, Bethany M. Niedzielski, Alexander Melville, Jonilyn L. Yoder, Cyrus F. Hirjibehedin, Terry P. Orlando, Simon Gustavsson, and William D. Oliver. Characterizing and optimizing qubit coherence based on squid geometry. *Phys. Rev. Applied*, 13:054079, May 2020.
  - [13] Jens Koch, Terri M. Yu, Jay Gambetta, A. A. Houck, D. I. Schuster, J. Majer, Alexandre Blais, M. H. Devoret, S. M. Girvin, and R. J. Schoelkopf. Charge-insensitive qubit design derived from the cooper pair box. *Phys. Rev. A*, 76:042319, Oct 2007.
  - [14] J. D. Strand, Matthew Ware, Félix Beaudoin, T. A. Ohki, B. R. Johnson, Alexandre Blais, and B. L. T. Plourde. First-order sideband transitions with flux-driven asymmetric transmon qubits. *Phys. Rev. B*, 87:220505, Jun 2013.
  - [15] M. D. Hutchings, J. B. Hertzberg, Y. Liu, N. T. Bronn, G. A. Keefe, Markus Brink, Jerry M. Chow, and B. L. T. Plourde. Tunable superconducting qubits with flux-independent coherence. *Phys. Rev. Applied*, 8:044003, Oct 2017.
  - [16] Simon Gustavsson, Jonas Bylander, Fei Yan, William D. Oliver, Fumiki Yoshihara, and Yasunobu Nakamura. Noise correlations in a flux qubit with tunable tunnel coupling. *Phys. Rev. B*, 84:014525, Jul 2011.
  - [17] M J Schwarz, J Goetz, Z Jiang, T Niemczyk, F Deppe, A Marx, and R Gross. Gradiometric flux qubits with a tunable gap. *New Journal of Physics*, 15(4):045001, apr 2013.
  - [18] See Supplementary Materials.
  - [19] Aaron D. O’Connell, M. Ansmann, R. C. Bialczak, M. Hofheinz, N. Katz, Erik Lucero, C. McKenney, M. Neeley, H. Wang, E. M. Weig, A. N. Cleland, and J. M. Martinis. Microwave dielectric loss at single photon energies and millikelvin temperatures. *Applied Physics Letters*, 92(11):112903, March 2008.
  - [20] G. Catelani, J. Koch, L. Frunzio, R. J. Schoelkopf, M. H. Devoret, and L. I. Glazman. Quasiparticle relaxation of superconducting qubits in the presence of flux. *Phys. Rev. Lett.*, 106:077002, Feb 2011.
  - [21] G. Catelani, R. J. Schoelkopf, M. H. Devoret, and L. I. Glazman. Relaxation and frequency shifts induced by quasiparticles in superconducting qubits. *Phys. Rev. B*, 84:064517, Aug 2011.
  - [22] Leonid I. Glazman and Gianluigi Catelani. Bogoliubov Quasiparticles in Superconducting Qubits. *SciPost Phys. Lect. Notes*, page 31, 2021.
  - [23] Ioan M. Pop, Kurtis Geerlings, Gianluigi Catelani, Robert J. Schoelkopf, Leonid I. Glazman, and Michel H. Devoret. Coherent suppression of electromagnetic dissipation due to superconducting quasiparticles. *Nature*, 508(7496):369–372, April 2014.
  - [24] Simon Gustavsson, Fei Yan, Gianluigi Catelani, Jonas Bylander, Archana Kamal, Jeffrey Birenbaum, David Hover, Danna Rosenberg, Gabriel Samach, Adam P. Sears, Steven J. Weber, Jonilyn L. Yoder, John Clarke, Andrew J. Kerman, Fumiki Yoshihara, Yasunobu Nakamura, Terry P. Orlando, and William D. Oliver. Suppressing relaxation in superconducting qubits by quasiparticle pumping. *Science*, 354(6319):1573–1577, December 2016.
  - [25] R. W. Simmonds, K. M. Lang, D. A. Hite, S. Nam, D. P. Pappas, and John M. Martinis. Decoherence in josephson phase qubits from junction resonators. *Phys. Rev. Lett.*, 93:077003, Aug 2004.
  - [26] J. Eroms, L. C. van Schaarenburg, E. F. C. Driessen, J. H. Plantenberg, C. M. Huizinga, R. N. Schouten, A. H. Verbruggen, C. J. P. M. Harmans, and J. E. Mooij. Low-frequency noise in josephson junctions for superconducting qubits. *Applied Physics Letters*, 89(12):122516, September 2006.
  - [27] G. Ithier, E. Collin, P. Joyez, P. J. Meeson, D. Vion, D. Esteve, F. Chiarello, A. Shnirman, Y. Makhlin, J. Schrieffer, and G. Schön. Decoherence in a superconducting quantum bit circuit. *Phys. Rev. B*, 72:134519, Oct 2005.